Chemical Science

ROYAL SOCIETY OF CHEMISTRY

EDGE ARTICLE

View Article Online
View Journal | View Issue

Cite this: *Chem. Sci.*, 2022, **13**, 2778

All publication charges for this article have been paid for by the Royal Society of Chemistry

Received 24th December 2021
Accepted 6th February 2022

DOI: 10.1039/d1sc07178e

rsc.li/chemical-science

Evolution from superatomic $Au_{24}Ag_{20}$ monomers into molecular-like $Au_{43}Ag_{38}$ dimeric nanoclusters†

Jiayu Xu,‡[a] Lin Xiong,‡[b] Xiao Cai,[a] Shisi Tang,[a] Ancheng Tang,[a] Xu Liu,[a] Yong Pei *[b] and Yan Zhu *[a]

Hierarchical assembly of nanoparticles has been attracting wide interest, as advanced functionalities can be achieved. However, the ability to manipulate structural evolution of artificial nanoparticles into assemblies with atomic precision has been largely unsuccessful. Here we report the evolution from monomeric $Au_{24}Au_{20}$ into dimeric $Au_{43}Ag_{38}$ nanoclusters: $Au_{43}Ag_{38}$ inherits the kernel frameworks from parent $Au_{24}Ag_{20}$ but exhibits distinct surface motifs; $Au_{24}Ag_{20}$ is racemic, while $Au_{43}Ag_{38}$ is mesomeric. Importantly, the evolution from monomers to dimers opens up exciting opportunities exploring currently unknown properties of monomeric and dimeric alloy nanoclusters. The $Au_{24}Ag_{20}$ clusters show superatomic electronic configurations, while $Au_{43}Ag_{38}$ clusters have molecular-like characteristics. Furthermore, monomeric $Au_{24}Ag_{20}$ catalysts readily outperform dimeric $Au_{43}Ag_{38}$ catalysts in the catalytic reduction of CO_2.

Introduction

Nanoparticle assembly in nanoscience and nanotechnology is important because of the exceptional properties produced that can serve for fundamental investigations and new applications.[1–9] Despite the impressive advances in the assembly of artificial nanoparticles, the precise assembly of nanoparticles with atomic-scale manipulation remains a great challenge. This hinders researchers from creating and optimizing the functionality of nanomaterials. The key requirement for achieving such assemblies is the formation of truly atomically defined particles. Metal nanoclusters with absolutely precise formulae and atomic structures have provided access to currently challenging issues regarding conventional nanoparticles.

In a series of seminal studies, gold or silver nanoclusters with icosahedral structures have been demonstrated to be basic building blocks forming the hierarchical assembly of nanoclusters with elegant structures. For example, $Au_{38}(SR)_{24}$ with a double-icosahedral Au_{23} kernel is assembled from two icosahedral Au_{13} units in a coplanar manner.[10,11] $[Au_{25}(PPh_3)_{10}(SR)_5Cl_2]^{2+}$ is evolved from two Au_{13} icosahedra sharing one vertex and $[Au_{37}(PPh_3)_{10}(SR)_{10}X_2]^+$ is formed by three Au_{13} icosahedra sharing vertices in a linear form.[12,13] Recently $Ag_{61}(dpa)_{27}(SbF_6)_4$ was found to contain four linear vertex-sharing Ag_{13} icosahedra.[14] Similarly, the cores of both $Au_2Ag_{42}(SAdm)_{27}(BPh_4)$ and $[Au_2Ag_{48}(S\text{-}tBu)_{20}(Dppm)_6Br_{11}]Br(BPh_4)_2$ are composed of two icosahedral Ag_{13} units.[15] Besides icosahedral $M_2Au_{36}(PET)_{24}$ was reported from the structural fusion of $[HMAu_8(PPh_3)_8]^+$ and $[MAu_{24}(PET)_{18}]^-$.[16] $Ag_2Au_{50}(SR)_{36}$ was synthesized from two $Au_{25}(SR)_{18}$ units assembled with two Ag atoms in a hand-in-hand mode.[17] These studies are exciting in the rational design and fabrication of tailored structures and reveal that the perfect nanocluster assembly deserves more efforts to tailor the functionality on an atom-by-atom basis.[18–21]

In this work, we successfully synthesized monomeric $Au_{24}Ag_{20}(C_{12}H_{13})_{24}Cl_2$ and $Au_{24}Ag_{20}(C_9H_7)_{24}Cl_2$ nanoclusters with similar kernels comprised of a hollow Au_{12} icosahedron surrounded by fullerene-like Ag_{20}. The two $Au_{24}Ag_{20}$ monomers are further fused along different pathways into the $Au_{12}@Ag_{19}$-Au-$Au_{12}@Ag_{19}$ kernels and finally form $Au_{43}Ag_{38}(C_{12}H_{13})_{36}Cl_{12}$ and $Au_{43}Ag_{38}(C_9H_7)_{36}Cl_9$ dimeric nanoclusters, respectively. The $Au_{24}Ag_{20}$ monomers and $Au_{43}Ag_{38}$ dimers offer a novel platform for atomic manufacturing on alloy nanoclusters to construct harmonious structures and unveil currently elusive properties such as electronic structures and catalytic properties.

Results and discussion

As shown in Fig. 1, based on a "cluster to cluster" strategy, four nanoclusters can be synthesized. $AuSMe_2Cl$ and CH_3COOAg precursors were reduced by $C_4H_{14}BN$ in the presence of 4-*tert*-butylphenylacetylene and sodium methoxide.

[a]*School of Chemistry and Chemical Engineering, Nanjing University, Nanjing 210093, China. E-mail: zhuyan@nju.edu.cn*

[b]*Department of Chemistry, Key Laboratory of Environmentally Friendly Chemistry and Applications of Ministry of Education, Xiangtan University, Xiangtan 411105, China. E-mail: ypnku78@gmail.com*

† Electronic supplementary information (ESI) available. CCDC 2129383–2129386. For ESI and crystallographic data in CIF or other electronic format see DOI: 10.1039/d1sc07178e

‡ These authors contributed equally to this work.

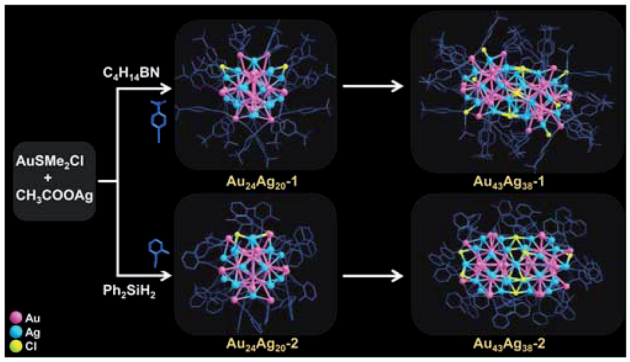

Fig. 1 Synthetic scheme of monomeric $Au_{24}Ag_{20}(C_{12}H_{13})_{24}Cl_2$ and $Au_{24}Ag_{20}(C_9H_7)_{24}Cl_2$ and dimeric $Au_{43}Ag_{38}(C_{12}H_{13})_{36}Cl_{12}$ and $Au_{43}Ag_{38}(C_9H_7)_{36}Cl_9$. $C_{12}H_{13}$ = deprotonated 4-*tert*-butylphenylacetylene, C_9H_7 = deprotonated 2-methylphenylacetylene. H atoms are omitted for clarity.

$Au_{24}Ag_{20}(C_{12}H_{13})_{24}Cl_2$ (abbreviated as $Au_{24}Ag_{20}$-1) was formed in a 12 hour reaction and then transformed into $Au_{43}Ag_{38}(C_{12}H_{13})_{36}Cl_{12}$ (abbreviated as $Au_{43}Ag_{38}$-1) in another 12 hour reaction. With 2-methylphenylacetylene as the ligand and diphenylsilane as the reducing agent, $Au_{24}Ag_{20}(C_9H_7)_{24}Cl_2$ (denoted as $Au_{24}Ag_{20}$-2) was first obtained and further converted to $Au_{43}Ag_{38}(C_9H_7)_{36}Cl_9$ (denoted as $Au_{43}Ag_{38}$-2).

Electrospray ionization mass (ESI-MS) and matrix-assisted laser desorption/ionization time of flight mass (MALDI-TOF-MS) spectrometry were carried out to confirm the cluster formula. The major peaks of monomers at m/z = 10 995 and 9719 were assigned to $[Au_{24}Ag_{20}(C_{12}H_{13})_{24}Cl_2 + 2Cs^+]^{2+}$ and $[Au_{24}Ag_{20}(C_9H_7)_{24}Cl_2 - 2e]^{2+}$ (Fig. S1†), respectively. The mass peaks of dimers at m/z = 18 500 and 16 916 were related to $Au_{43}Ag_{38}(C_{12}H_{13})_{35}Cl_{12}$ and $Au_{43}Ag_{38}(C_9H_7)_{35}Cl_9$ (Fig. S2;† note that one alkyne ligand for $Au_{43}Ag_{38}$ was removed during the measurements), respectively. The total structures of the four clusters were determined by X-ray crystallography (Tables S1–S4†). Among them, the two monomers have identical kernels of $Au_{12}@Ag_{20}$, which can be viewed as a hollow Au_{12} icosahedral structure surrounded by a fullerene-like Ag_{20} shell (Fig. 2A). The kernels of dimers are generated by the fusion of two $Au_{12}@Ag_{20}$ units of monomers in a mode of $Au_{12}@Ag_{19}$–Au–$Au_{12}@Ag_{19}$ (Fig. 2). This is completely different from previous cases, in which the building blocks of nanoclusters are mainly based on icosahedral units.

In terms of the monomers, the average Au–Au bond lengths of the Au_{12} icosahedral cores are very close (2.786 Å for $Au_{24}Ag_{20}$-1 and 2.785 Å for $Au_{24}Ag_{20}$-2). As shown in Fig. S3,† the average Au–Ag bond lengths between the Au_{12} core and Ag_{20} shell are 2.878 Å in $Au_{24}Ag_{20}$-1 and 2.868 Å in $Au_{24}Ag_{20}$-2, respectively, and both are shorter than those of bulk Au or bulk Ag, implying the strong metal bonding between the Au_{12} core and Ag_{20} shell. Of note, the Au–Au distances between the Au_{12} core and outer Au_{12} shell and between the Ag_{20} shell and outer Au_{12} shell are longer than those of bulk Au and Ag, indicating the weak interaction between the outermost Au atoms and Ag_{20} shell. Obviously, the surface arrangements of the two $Au_{24}Ag_{20}$ nanoclusters are different. $Au_{24}Ag_{20}$-1 has four binding types on

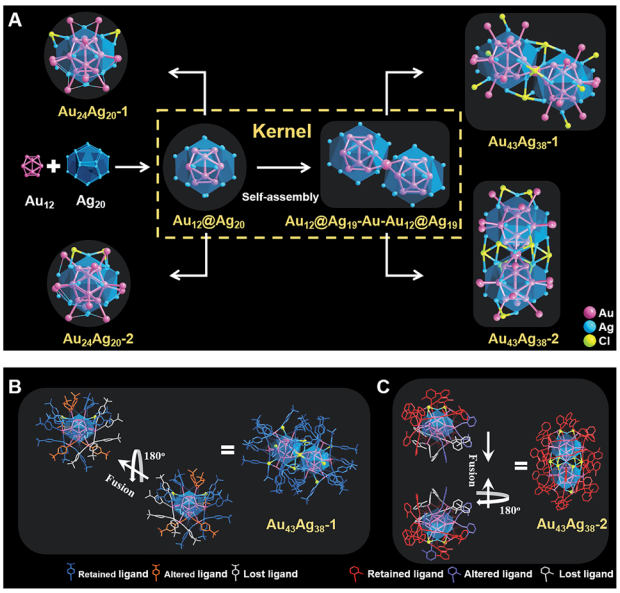

Fig. 2 (A) The kernel anatomy of $Au_{24}Ag_{20}$ containing a hollow Au_{12} icosahedron surrounded by fullerene-like Ag_{20} and the kernel anatomy of $Au_{43}Ag_{38}$ fused from two $Au_{12}@Ag_{20}$ units sharing a Au atom that replaces a Ag atom. The assembly pathways of (B) $Au_{43}Ag_{38}$-1 and (C) $Au_{43}Ag_{38}$-2 dimers evolved from the $Au_{24}Ag_{20}$ monomers.

the Ag_5 faces (Fig. S4A–D†), while $Au_{24}Ag_{20}$-2 has three binding structures on the Ag_5 faces (Fig. S4E–G†), although both $Au_{24}Ag_{20}$ nanoclusters exhibit such coordination modes on the staples: 12 as η_3-μ_1(Au), μ_2(Ag), and μ_2(Ag) and 12 as η_2-μ_1(Au) and μ_2(Ag). The different binding motifs also lead to distinguishable steric arrangements of two Au and two Cl atoms at the top of the $Au_{24}Ag_{20}$ nanoclusters: symmetrically upward to form two parallel staples for $Au_{24}Ag_{20}$-1 (upper panel of Fig. 3); distinctively twisted to form two crossed staples for $Au_{24}Ag_{20}$-2 (lower panel of Fig. 3). The specific staples of the two nanoclusters might be acting as identification cards for identifying changes that have taken place in subsequent polymerizations.

With respect to the dimers, their kernel structures are alike. The average Au–Au bond lengths of the Au_{12}–Au–Au_{12} core are

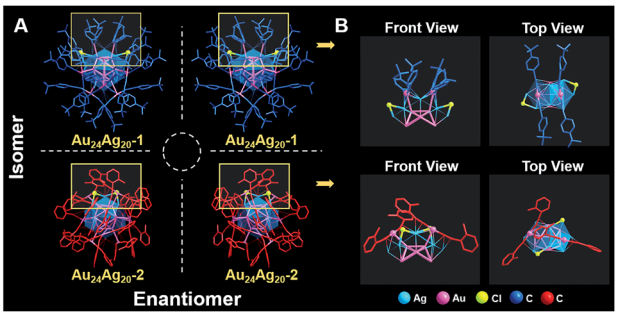

Fig. 3 (A) Two enantiomers of $Au_{24}Ag_{20}$-1 (upper panel); two enantiomers of $Au_{24}Ag_{20}$-2 (lower panel). (B) The specific staples and corresponding steric configurations of $Au_{24}Ag_{20}$: two parallel staples and two Cl arrangements for $Au_{24}Ag_{20}$-1 (upper panel); two crossed staples and two Cl arrangements for $Au_{24}Ag_{20}$-2 (lower panel).

2.790 Å in $Au_{43}Ag_{38}$-1 and 2.789 Å in $Au_{43}Ag_{38}$-2. The lengths of the Au–Au bonds directly connected to the central gold are the shortest in the whole core (Fig. S5†). The average Au–Ag lengths between the Au_{12}–Au–Au_{12} core and Ag_{38} shell are 2.891 Å in $Au_{43}Ag_{38}$-1 and 2.911 Å in $Au_{43}Ag_{38}$-2, suggesting the weak interaction between the Au core and Ag shell, which differs from the monomeric cases. Additionally, the average Au–Au distances between the Au_{12}–Au–Au_{12} core and outer Au_{18} shell are 2.856 Å in $Au_{43}Ag_{38}$-1 and 2.883 Å in $Au_{43}Ag_{38}$-2, suggesting strong a Au–Au force on the outer shell. The Au–Ag distances between the Ag_{38} shell and outer Au_{18} shell are longer than 3 Å for both $Au_{43}Ag_{38}$ nanoclusters and are consistent with the monomers. Moreover, clearly discernible surface motifs are presented in the $Au_{43}Ag_{38}$ clusters: $Au_{43}Ag_{38}$-1 has four binding types on the Ag_5 faces with the coordination modes (Fig. S6†): 22 as η_3-μ_1(Au), μ_2(Ag), and μ_2(Ag) and 14 as η_2-μ_1(Au) and μ_2(Ag); $Au_{43}Ag_{38}$-2 has five binding types on the Ag_5 faces with the coordination modes (Fig. S7†): 24 as η_3-μ_1(Au), μ_2(Ag), and μ_2(Ag) and 12 as η_2-μ_1(Au), μ_2(Ag). Both dimers contain 36 alkyne ligands, but $Au_{43}Ag_{38}$-1 has 12 Cl and $Au_{43}Ag_{38}$-2 has only 9 Cl. In addition, both dimers have six four-coordinated Cl atoms, but $Au_{43}Ag_{38}$-1 has another six one-coordinated Cl atoms and $Au_{43}Ag_{38}$-2 has another three two-coordinated Cl atoms. More interestingly, the specific staples as identification cards can also be found in the two dimeric nanoclusters (Fig. 4): the parallel staples on $Au_{43}Ag_{38}$-1 and the crossed staples on $Au_{43}Ag_{38}$-2.

It is worth pointing out that the unit cell of each $Au_{24}Ag_{20}$ monomer comprises two enantiomers, and hence the monomers are racemic (Fig. 3A). One $Au_{24}Ag_{20}$ isomer rotates 180° and then fuses with the other isomer by four or six Cl linkages to form $Au_{43}Ag_{38}$, in which two fusion units are chiral and the total $Au_{43}Ag_{38}$ clusters are thus mesomeric (Fig. 4A). Remarkably, $Au_{43}Ag_{38}$-1 is assembled from two chiral units along the diagonal direction, while $Au_{43}Ag_{38}$-2 is evolved from the vertical fusion of two chiral units. During the fusion process, each fusion unit of $Au_{43}Ag_{38}$-1 shows 5 alkyne rearranged, 6 alkyne detached and 4 Cl added (upper panel of Fig. 4A). However, when the fusion process happened to $Au_{43}Ag_{38}$-2, one fusion unit has 5 alkyne relocated, 6 alkyne left and 3 Cl fixed, whereas the other fusion unit shows 6 alkyne relocated, 6 alkyne and one Cl fell off, and another 3 Cl appended (lower panel of Fig. 4A).

We next compared the electronic properties of monomeric and dimeric nanoclusters. The UV-vis absorption spectra of $Au_{24}Ag_{20}$ show four apparent peaks, while those of $Au_{43}Ag_{38}$ show five absorption peaks (Fig. S8†). It implies different electronic structures between monomers and dimers. We further performed density functional theory (DFT) calculations on the electronic configuration of these nanoclusters. From Fig. 5A, it is obvious that the Kohn–Sham (KS) orbital diagram of the $Au_{24}Ag_{20}$ monomer is similar to that of the orbitals of atoms, with the characteristics of s, p, d, and f atomic orbitals. Considering that $Au_{24}Ag_{20}$ has 18 valence electrons, it just forms an electron shell of $1s^2|1p^6|1d^{10}$, which is identical to the KS electron density diagram of typical superatomic $Au_{25}(SR)_{18}^-$ (Fig. S9A and B†).[22] Therefore, $Au_{24}Ag_{20}$ can be classified into the category of superatomic clusters. Surprisingly, $Au_{43}Ag_{38}$ and $Au_{38}(SR)_{24}$ exhibit similar molecular orbital types (Fig. 5B, S9C and D†): bonding orbitals σ and π; anti-bonding orbitals σ* and π*.[23] Obviously, these molecular orbitals can be viewed as linear combinations of different atomic orbitals of $Au_{24}Ag_{20}$ in different ways (head-to-head combination to obtain σ orbitals and side-to-side combination to form π orbitals). It is noted that due to the influence of the outer layer ligand, the molecular orbital diagram of the overall structure of $Au_{43}Ag_{38}$ and the orbital diagram of the inner core structure are different, *e.g.*, the molecular orbital of the inner core has a δ orbital (Fig. S9D†). Nevertheless, this does not affect our qualitative judgement on the properties of the molecule. Overall, the configurations that can form superatoms are not only icosahedral but also diversified, and even alloy clusters also have superatomic or molecular-like characteristics.

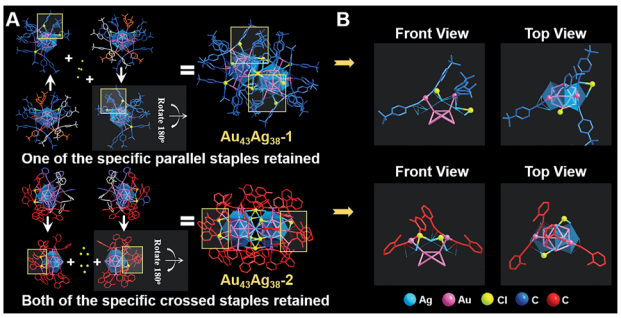

Fig. 4 (A) Fusion of isomeric $Au_{24}Ag_{20}$ into $Au_{43}Ag_{38}$ containing chiral units. (B) The distinct staples and corresponding steric configurations of the $Au_{43}Ag_{38}$ nanoclusters: two parallel staples and two Cl position for $Au_{43}Ag_{38}$-1 (upper panel); two crossed staples and two Cl position for $Au_{43}Ag_{38}$-2 (lower panel).

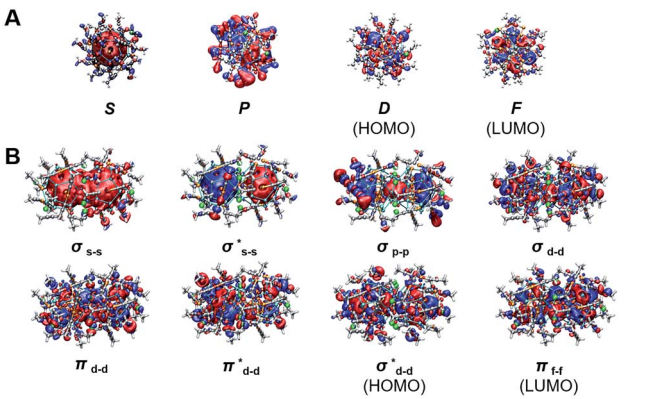

Fig. 5 The Kohn–Sham orbital diagrams of (A) $Au_{24}Ag_{20}$ and (B) $Au_{43}Ag_{38}$. Simplified calculations with methyl as a substituent. The subscript in the molecular orbital symbol indicates the type of atomic orbital that is linearly combined into molecular orbitals. The head-to-head overlap of p atomic orbitals leads to bonded (σ_{p-p}) and anti-bonded (σ^*_{d-d}) molecular orbitals, where the electron density is centered along the internuclear axis, making them σ orbitals. The π_{d-d} and π^*_{d-d} orbitals are a linear combination of two d atomic orbitals side-to-side. HOMO: highest occupied molecular orbital. LUMO: lowest unoccupied molecular orbital.

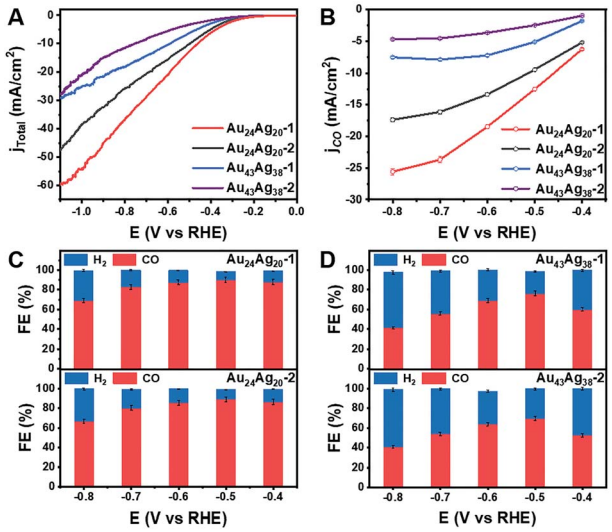

Fig. 6 (A) LSV curves of the $Au_{24}Ag_{20}$ and $Au_{43}Ag_{38}$ cluster catalysts in a CO_2-saturated 0.5 M $KHCO_3$ solution. (B) The corresponding CO partial current density. (C) Faradaic efficiency for CO_2RR products obtained on $Au_{24}Ag_{20}$. (D) Faradaic efficiency for CO_2RR products obtained on $Au_{43}Ag_{38}$.

More importantly, the inherent ability of electron transport in monomeric and dimeric nanoclusters is readily differentiated in their electrochemical impedance spectra (Fig. S10†). The semicircular diameters of the $Au_{24}Ag_{20}$ clusters are smaller than those of the $Au_{43}Ag_{38}$ clusters, meaning that the electron transport in the monomers might be faster than that in the dimers. Given the inherent advantages of employing the cluster catalysts in electronic properties, we envisioned the CO_2 reduction reaction (CO_2RR) involving the electron transfer process to explore the catalytic properties of the monomers and dimers. We were pleased to observe different reactivities of the four nanocluster catalysts for the CO_2RR and the high performances were achieved in the monomers. From the linear scanning voltammetry (LSV) curves of $Au_{24}Ag_{20}$ and $Au_{43}Ag_{38}$ in CO_2-saturated solutions of 0.5 M $KHCO_3$, the monomers showed higher current density than the dimers (Fig. 6A). Meanwhile, the CO partial current density was arranged in descending order as $Au_{24}Ag_{20}$-1 > $Au_{24}Ag_{20}$-2 > $Au_{43}Ag_{38}$-1 > $Au_{43}Ag_{38}$-2 (Fig. 6B). Notably, the monomers showed much higher faradaic efficiency (FE) toward CO than the dimers in the voltage range from −0.4 to −0.8 V (Fig. 6C and D). 90% CO FE was obtained at a voltage of −0.5 V over the $Au_{24}Ag_{20}$ catalysts. The results were partially related to their atomic-packing structures (individual-core *vs.* dual-core) and surface motif arrangements (parallel *vs.* crossed).[24,25] Further studies are ongoing to elucidate the roles of superatomic and molecular-like electronic properties on cluster catalysis, which so far remain elusive.

Conclusions

In summary, we have successfully implemented the evolution of racemic $Au_{24}Ag_{20}$ monomers into mesomeric $Au_{43}Ag_{38}$ dimers and mapped out significant differences in steric configurations and electronic structures between the monomeric and dimeric nanoclusters. Our studies show that the $Au_{24}Ag_{20}$ monomers exhibit more efficient reactivity than the $Au_{43}Ag_{38}$ dimers for CO_2 reduction processes. This work not only provides a strategy for hierarchical assembly of metal nanoclusters to tune their structure and functionality, but also provides a paradigm of the monomeric and dimeric alloy nanoclusters to find applications in challenging chemical reactions.

Data availability

The X-ray crystallographic structures reported in this article have been deposited at the Cambridge Crystallographic Data Centre (CCDC) with deposition numbers (CCDC: 2129383 for $Au_{43}Ag_{38}(C_{12}H_{13})_{36}Cl_{12}$; CCDC: 2129384 for $Au_{24}Ag_{20}(C_9H_7)_{24}Cl_2$; CCDC: 2129385 for $Au_{43}Ag_{38}(C_9H_7)_{36}Cl_9$; CCDC: 2129386 for $Au_{24}Ag_{20}(C_{12}H_{13})_{24}Cl_2$).

Author contributions

Y. Z. conceived the project. J. X. synthesized the nanoclusters and grew the crystal. L. X. and Y. P. conducted the calculations. X. C. and S.T. did the catalytic tests. A. T. and X. L. analyzed the crystal data. All authors wrote the manuscript.

Conflicts of interest

There are no conflicts to declare.

Acknowledgements

We acknowledge financial support from National Natural Science Foundation of China (22125202; 91961121) and Programs for High-Level Entrepreneurial and Innovative Talents Introduction of Jiangsu Province.

Notes and references

1 T. Wang, J. Zhuang, J. Lynch, O. Chen, Z. Wang, X. Wang, D. LaMontagne, H. Wu, Z. Wang and Y. C. Cao, *Science*, 2012, **338**, 358–363.
2 C. Zeng, Y. Chen, K. Kirschbaum, K. J. Lambright and R. Jin, *Science*, 2016, **354**, 1580–1584.
3 Z. Lei, X. Pei, Z. Jiang and Q. Wang, *Angew. Chem., Int. Ed.*, 2014, **53**, 12771–12775.
4 I. Chakraborty and T. Pradeep, *Chem. Rev.*, 2017, **117**, 8208–8271.
5 Y. Song, F. Fu, J. Zhang, J. Chai, X. Kang, P. Li, S. Li, H. Zhou and M. Zhu, *Angew. Chem., Int. Ed.*, 2015, **54**, 8430–8434.
6 R. Huang, Y. Wei, X. Dong, X. Wu, C. Du, S. Zang and T. C. W. Mak, *Nat. Chem.*, 2017, **9**, 689–697.
7 L. Shi, L. Zhu, J. Guo, L. Zhang, Y. Shi, Y. Zhang, K. Hou, Y. Zheng, Y. Zhu, J. Lv, S. Liu and Z. Tang, *Angew. Chem., Int. Ed.*, 2017, **56**, 15397–15401.
8 Z. Wang, M. Wang, Y. Li, P. Luo, T. Jia, R. Huang, S. Zang and T. C. W. Mak, *J. Am. Chem. Soc.*, 2018, **140**, 1069–1076.

9 G. Deng, B. K. Teo and N. Zheng, *J. Am. Chem. Soc.*, 2021, **143**, 10214–10220.
10 H. Qian, W. T. Eckenhoff, Y. Zhu, T. Pintauer and R. Jin, *J. Am. Chem. Soc.*, 2010, **132**, 8280–8281.
11 Y. Pei, Y. Gao and X. Zeng, *J. Am. Chem. Soc.*, 2008, **130**, 7830–7832.
12 Y. Shichibu, Y. Negishi, T. Watanabe, N. K. Chaki, H. Kawaguchi and T. Tsukuda, *J. Phys. Chem. C*, 2007, **111**, 7845–7847.
13 R. Jin, C. Liu, S. Zhao, A. Das, H. Xing, C. Gayathri, Y. Xing, N. L. Rosi, R. R. Gil and R. Jin, *ACS Nano*, 2015, **9**, 8530–8536.
14 S. Yuan, C. Xu, W. Liu, J. Zhang, J. Li and Q. Wang, *J. Am. Chem. Soc.*, 2021, **143**, 12261–12267.
15 S. Jin, X. Zou, L. Xiong, W. Du, S. Wang, Y. Pei and M. Zhu, *Angew. Chem., Int. Ed.*, 2018, **57**, 16768–16772.
16 E. Ito, S. Takano, T. Nakamura and T. Tsukuda, *Angew. Chem., Int. Ed.*, 2021, **60**, 645–649.
17 X. Liu, G. Saranya, X. Huang, X. Cheng, R. Wang, M. Chen, C. Zhang, T. Li and Y. Zhu, *Angew. Chem., Int. Ed.*, 2020, **59**, 13941–13946.
18 Z. Lei, J. Li, Z. Nan, Z. Jiang and Q. Wang, *Angew. Chem., Int. Ed.*, 2021, **60**, 14415–14419.
19 P. Yuan, R. Zhang, E. Selenius, P. Ruan, Y. Yao, Y. Zhou, S. Malola, H. Häkkinen, B. K. Teo, Y. Cao and N. Zheng, *Nat. Commun.*, 2020, **11**, 2229.
20 Z. Wu, Y. Du, J. Liu, Q. Yao, T. Chen, Y. Cao, H. Zhang and J. Xie, *Angew. Chem., Int. Ed.*, 2019, **58**, 8139–8144.
21 M. D. Nardi, S. Antonello, D.-E. Jiang, F. Pan, K. Rissanen, M. Ruzzi, A. Venzo, A. Zoleo and F. Maran, *ACS Nano*, 2014, **8**, 8505–8512.
22 C. M. Aikens, *Acc. Chem. Res.*, 2018, **51**, 3065–3073.
23 Q. Tang, G. Hu, V. Fung and D.-E. Jiang, *Acc. Chem. Res.*, 2018, **51**, 2793–2802.
24 H. Seong, V. Efremov, G. Park, H. Kim, J. S. Yoo and D. Lee, *Angew. Chem., Int. Ed.*, 2021, **60**, 14563–14570.
25 M. R. Narouz, K. M. Osten, P. J. Unsworth, R. W. Y. Man, K. Salorinne, S. Takano, R. Tomihara, S. Kaappa, S. Malola, C. Dinh, J. D. Padmos, K. Ayoo, P. J. Garrett, M. Nambo, J. H. Horton, E. H. Sargent, H. Häkkinen, T. Tsukuda and C. M. Crudden, *Nat. Chem.*, 2019, **11**, 419–425.